Supporting Information: The Role of Different Energy Portions on the 2D/3D Stability Swapping for 13–Atoms Metal Clusters

Diego Guedes-Sobrinho,[*,†] Renato P. Orenha,[‡] Renato L. T. Parreira,[‡] Glaucio R. Nagurniak,[¶] Gabriel Reynald Da Silva,[†] and Maurício J. Piotrowski[*,§]

†*Chemistry Department, Federal University of Paraná, CEP 81531-980, Curitiba, Brazil*

‡*Núcleo de Pesquisas em Ciências Exatas e Tecnológicas, Universidade de Franca, Franca, SP, Brazil*

¶*Chemistry Department, Universidade Estadual de Ponta Grossa, Ponta Grossa, PR Brazil*

§*Department of Physics, Federal University of Pelotas, PO Box* 354, 96010-900*, Pelotas, RS, Brazil*

E-mail: guedessobrinho@ufpr.br; mauriciomjp@gmail.com

Phone: +55(41)33613470; +55 53 3275 7542

Table S1: Convergence tests for the relative total energy, $\Delta E_{Tot}(eV)$, average weighted bond length, d_{av} (Å), effective coordination number, ECN, and total magnetic moment, m_T, with respect to the box size (L) used, where $L = 09, 11, 13, 15, 17, 19, 21$ Å.

L	DFT-PBE				DFT-PBE+D3				DFT-PBE+TS			
(Å)	ΔE_{Tot}	d_{av}	ECN	m_T	ΔE_{Tot}	d_{av}	ECN	m_T	ΔE_{Tot}	d_{av}	ECN	m_T
09	6.99228	2.7408	5.0239	1.00	7.76965	2.7823	5.4675	1.00	7.99959	2.7489	5.4562	1.00
11	0.00915	2.8740	6.3963	5.00	0.15943	2.8800	6.3965	5.00	0.14997	2.8664	6.3965	5.00
13	0.00233	2.8747	6.3965	5.00	0.04324	2.8795	6.3965	5.00	0.04768	2.8663	6.3965	5.00
15	0.00341	2.8747	6.3965	5.00	0.01876	2.8798	6.3965	5.00	0.02332	2.8665	6.3965	5.00
17	0.00330	2.8747	6.3965	5.00	0.00013	2.8791	6.3965	5.00	0.00221	2.8670	6.3965	5.00
19	0.00315	2.8747	6.3965	5.00	0.00155	2.8792	6.3965	5.00	0.00185	2.8666	6.3965	5.00
21	0.00000	2.8747	6.3965	5.00	0.00000	2.9793	6.3965	5.00	0.00000	2.8666	6.3965	5.00

I Computational Details

As implemented in VASP,[1–3] the Kohn–Sham equations were solved employing the all-electron projector augmented wave method[4,5] as implemented in VASP.[1–3] For all calculations, we employed a cubic box with a distance of 17 Å, which yields a minimum distance of 8 Å between the systems and their periodic images; and cutoff energies of 490 eV, 313 eV, and 384 eV for Cu_{13}, Ag_{13}, and Au_{13} clusters, respectively, which are larger by 25 % than the values recommended by VASP. We carry out convergence tests for the main computational parameters, for example, for the size of the box (used in the VASP simulation) to avoid interaction between the periodic images. In Table S1, we show the convergence tests with regard to box size by considering three approaches: DFT-PBE, DFT-PBE+D3 (empirical), and DFT-PBE+TS (semi empirical electronic density dependent) for Au_{13} as ICO, where the relative total energy is given in relation to the largest box size (21 Å). From these results, it is possible to verify that a box with a 17 Å side (producing a distance of 8 Å among the periodic images) is sufficiently precise to generate a good correspondence between cost and benefit.

For the Brillouin zone (BZ) integration, we have considered a single **k**-point (Γ-point) for the clusters since there is no dispersion of the electronic states along any direction within the BZ. For all calculations, the equilibrium geometries were obtained when the atomic forces on every atom were smaller than $0.01\,eV/Å$ with a total energy convergence criterion of 1.0×10^{-6} eV.

II Energetic Analysis for Au_{13} as a Fixed ICO Configuration with SOC

Figure S1 depicts the energy decomposition for Au_{13} for 2D and 3D with respect to the fixed icosahedral (ICO) structure.

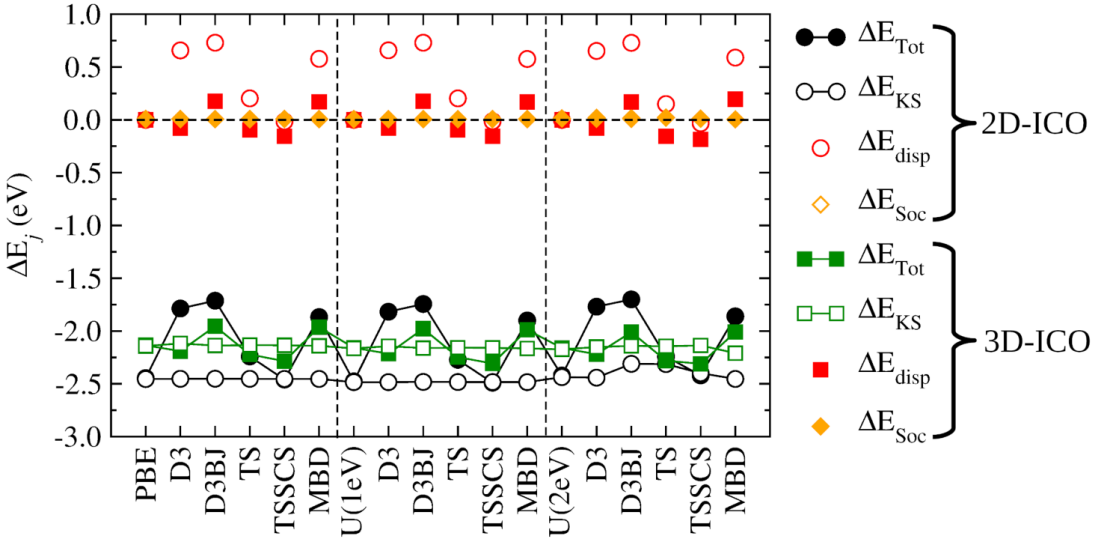

Figure S1: Relative total energy (ΔE_{Tot}), relative Kohn–Sham energy (ΔE_{KS}), and relative van der Waals energy (ΔE_{disp}) for Au_{13} calculations with SOC by including relative SOC energy (ΔE_{Soc}), between 2D–ICO^{fixed} and 3D–ICO^{fixed} configurations obtained by PBE+SOC combined with vdW, $+U$, and $+U$+vdW, where $U = 1.0$ and 2.0 eV, from which vdW is D3, D3BJ, TS, TSSCS, or MBD.

III Energy Decomposition Analysis

Below, we provided a figure (Figure S2) with the fragmentation model together with the graphical energy decomposition for the Cu_{13}, Ag_{13}, and Au_{13} clusters in the 2D, 3D, and ICO configurations, where the color atoms represent the fragment 1, while the rest of the atoms represent the fragment 2. In addition, we provided a table (Table S2) with the energy decomposition analysis (EDA).

To improve the understanding of how the local chemical environment (coordination), encompassed in geometries (2D, 3D, and ICO), affects the Cu_{13}, Ag_{13}, and Au_{13} bonding situation, we

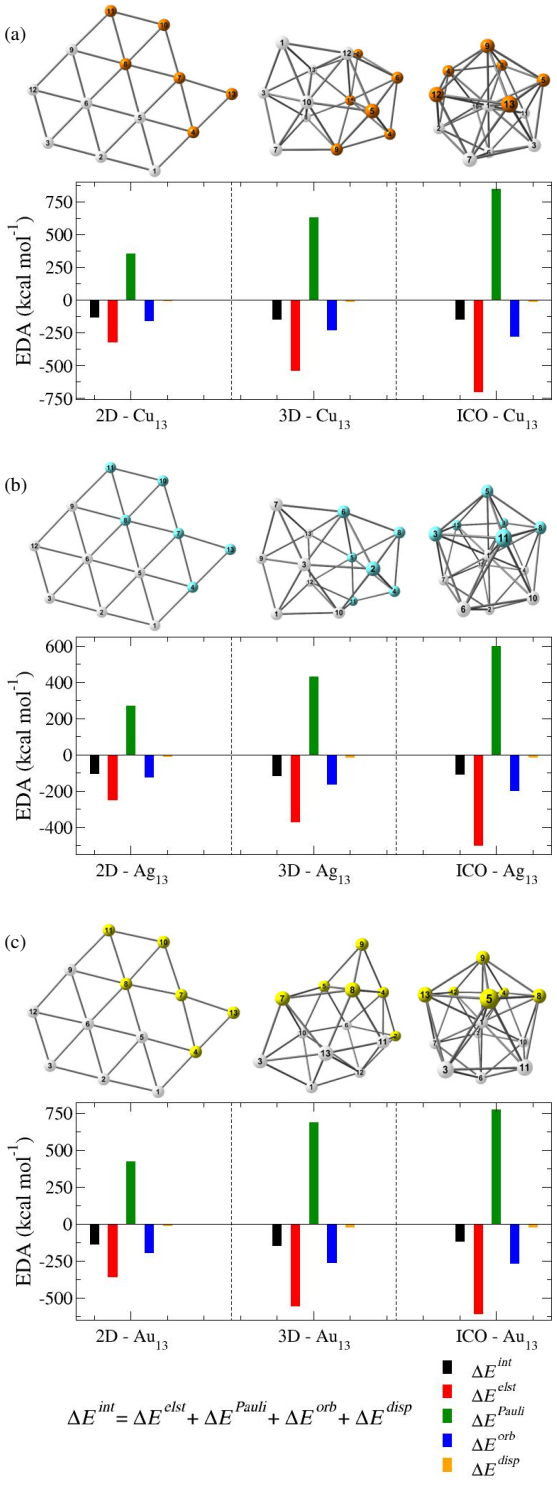

Figure S2: Fragmentation model for the (a) Cu_{13}, (b) Ag_{13}, and (c) Au_{13} clusters in the 2D, 3D, and ICO configurations and the respective energy decomposition analysis. Atoms colour code: Cu - orange, Ag - light blue, and Au - yellow.

Table S2: The EDA-NOCV analysis of 6– and 7–atom (where TM = Cu, Ag, and Au) fragment-interactions considering the 2D, 3D, and ICO configurations for Cu_{13}, Ag_{13}, and Au_{13} clusters, using PBE+D3-ZORA/TZP. All values are in kcal·mol^{-1}, except the values between parenthesis, which are the percentage contributions to ΔE^{int} (indicated by [a]), the percentage contribution to ΔE^{orb}_{tot} (indicated by [b]), and the Hirshfeld charges that are expressed in atomic units, where q_1 and q_2 denote the Hirshfeld charges of each fragment (indicated by [c]).

	2D - Cu_{13}	3D - Cu_{13}	ICO - Cu_{13}	2D - Ag_{13}	3D - Ag_{13}	ICO - Ag_{13}	2D - Au_{13}	3D - Au_{13}	ICO - Au_{13}
ΔE^{int}	−132.98	−146.41	−146.27	−104.77	−115.56	−107.54	−134.62	−146.67	−117.12
ΔE^{Pauli}	351.27	628.92	844.29	271.34	428.74	600.60	424.26	685.92	773.62
ΔE^{elst}	−319.13	−536.11	−700.20	−246.91	−368.08	−497.61	−355.90	−550.59	−603.46
[a] (%)	(65.90)	(69.15)	(70.69)	(65.65)	(67.62)	(70.27)	(63.68)	(66.13)	(67.75)
ΔE^{orb}_{tot}	−157.18	−226.77	−277.55	−121.79	−162.89	−196.57	−192.31	−262.20	−267.07
[a] (%)	(32.46)	(29.25)	(28.02)	(32.38)	(29.93)	(27.76)	(34.41)	(31.49)	(29.98)
ΔE^{disp}	−7.94	−12.45	−12.82	−7.41	−13.33	−13.97	−10.66	−19.80	−20.21
[a] (%)	(1.64)	(1.61)	(1.29)	(1.97)	(2.45)	(1.97)	(1.91)	(2.38)	(2.27)
ΔE^{orb}_{1}	−56.44	−71.54	−59.85	−48.23	−54.97	−37.15	−68.16	−63.65	−53.40
[b] (%)	(35.91)	(31.55)	(21.56)	(39.60)	(33.75)	(18.90)	(35.44)	(24.28)	(19.99)
ΔE^{orb}_{2}	−29.68	−33.99	−51.19	−26.03	−30.62	−46.43	−36.42	−46.18	−49.44
[b] (%)	(18.88)	(14.99)	(18.44)	(21.37)	(18.80)	(23.62)	(18.94)	(17.61)	(18.51)
ΔE^{orb}_{3}	−20.02	−25.20	−27.24	−15.06	−19.97	−31.57	−20.94	−37.45	−27.42
[b] (%)	(12.73)	(11.11)	(9.81)	(12.37)	(12.26)	(16.06)	(10.89)	(14.28)	(10.27)
ΔE^{orb}_{res}	−51.04	−96.04	−139.27	−32.47	−57.33	−81.42	−66.79	−114.92	−136.81
[b] (%)	(32.48)	(42.35)	(50.19)	(26.66)	(35.19)	(41.42)	(34.73)	(43.83)	(51.23)
[c] q_1	−0.0686	0.0084	−0.0933	−0.0752	0.0312	−0.0425	−0.0515	0.0276	−0.0064
[c] q_2	0.0687	−0.0084	0.0934	0.0753	−0.0312	0.0426	0.0516	−0.0276	0.0065

have measured the magnitude and nature of $Cu_6\cdots Cu_7$, $Ag_6\cdots Ag_7$, and $Au_6\cdots Au_7$ interactions. We carried out DFT-PBE+D3/TZP calculations considering the splitted cluster in sub-clusters, as two open-shell interacting fragments, subject to EDA-NOCV analysis. It is evidenced by the energy dataset that the stabilization energies between 6– and 7–atom fragments are in line with the overall energy order (relative total energies) for the coinage-metal clusters obtained from PBE+D3. The 3D configuration presented the largest bond magnitude between the fragments for all systems with ΔE^{3D}_{tot} values of -0.14 kcal·mol^{-1}, -8.02 kcal·mol^{-1}, and -29.55 kcal·mol^{-1}, while the ΔE^{2D}_{tot} values were given by 13.29 kcal·mol^{-1}, 2.77 kcal·mol^{-1}, and -17.50 kcal·mol^{-1}, respectively.

To facilitate the analysis, we have included the percentage values of contributions to ΔE^{int} term (indicated by [a] in Table S2), from which it is possible to observe the same well-established trend for the highest weight contributions, ΔE^{elst} and ΔE^{orb}_{tot}, for all systems in relation to the different

structural patterns. All clusters show primarily a significant Pauli repulsion term, followed by an expressive electrostatic character, and after, by a covalent feature, where the ΔE^{elst} percentage contributions follow the 2D<3D<ICO trend, while the ΔE^{orb}_{tot} percentage contributions have an opposite trend, i.e., 2D>3D>ICO. Consequently, we observe that the interaction-intensifications between the fragments of the 3D structure, which lead to their greater stabilization in relation to other structural motifs, is not attributed to the prominence in any of the most contributory terms of ΔE^{int}, but rather, by an intermediate relief of steric repulsion and by the energy balance of ionic and covalent contributions in the cohesive interactions of the 3D structure.

It can be seen that the ionic character is dominant in structures with a more packed chemical environment (close-packed configurations, e.g., ICO), i.e., the largest energy contributions of the electrostatic term (ΔE^{elst}) are managed in accordance with the larger coordination of structural models, for the clusters of the three congener elements. The covalent character (ΔE^{orb}_{tot}), on the other hand, stands out in 2D structures, with a rich overlap of fragment orbitals, which can be justified by the directional character of chemical bonds being quite evident in order to fulfill the planarity of this structural model. Within this conjecture, the 3D structure presents itself as an intermediary structural model between the 2D and ICO geometries, reaching the energetic balance of the contributions between a more ionic and a more covalent character, showing itself as the preferred structural pattern for the three coinage-metals.

Another factor that corroborates the stabilization of the 3D structure, to a lesser extent, concerns the percentage values of ΔE^{disp}, which reach values between 1.29 (ICO – Cu_{13}) and 2.45 % (3D – Ag_{13}). Overall, the 3D structure has the most salient dispersive contributions, with the exception of Cu_{13} clusters where the ΔE^{disp} percentage has similar values for both 2D and 3D structures. Thus, this result reinforces the larger energetic improvement of the 3D structure by vdW corrections, which would be equivalent to elucidate a higher sensitivity of these structures in relation to dispersive corrections.

In Table S2 we also observe the decomposition of the covalency degree, given by ΔE^{orb}_{tot}, into sub-terms representing the different types of covalent bondings, more specifically, σ, π, δ, among

others. For all clusters, it was obtained more than 10 sub-terms of ΔE_{tot}^{orb}, however, the first three terms are shown in Table S2, since they are the most energetically significant, while the remaining ones were grouped in the ΔE_{res}^{orb} term and are considered as polarization terms. Analyzing the percentage contribution to ΔE_{tot}^{orb} (indicated by ^{b} in Table S2) we observe that there is a similar trend for the three systems along the structural models, where the σ bond character, shown in ΔE_{1}^{orb}, follows the 2D>3D>ICO trend, corroborating the more covalent character present in 2D structures with planar directionality. In contrast, we observe that the orbital residual terms (grouped in ΔE_{res}^{orb}), which contribute to the polarization, show a trend for all systems given by 2D<3D<ICO, consequently, larger ΔE_{res}^{orb} term represents a more spread out charge flux in full correlation with higher coordination number. Therefore, we need to highlight again that the 3D structure can be found in a balance level between an exacerbated covalent character (2D) and a huge polarization effect (ICO).

Finally, we can also show the smaller π binding character (ΔE_{2}^{orb}) for the 3D structural model in relation to the other patterns, followed by a not very clear trend for the ΔE_{3}^{orb} contributions. It is also worth mentioning that the Hirshfeld charge analysis showed just a few amount of charge exchanged between sub-cluster fragments, being used much more as a check analysis.

Table S3: Hybridization index (h) for the Cu_{13}, Ag_{13}, and Au_{13} clusters in anum2D, ICO, and 3D configurations through all protocols employed, i.e., PBE, PBE+vdW, PBE+SOC, PBE+SOC+vdW, PBE+U, PBE+U+vdW, PBE+U+SOC, and PBE+U+SOC+vdW, where $U = 1.0$ and $2.0\,\mathrm{eV}$ and vdW is equal to D3, D3BJ, TS, TSSCS, or MBD. For SOC calculations of the Au_{13} clusters, the ICO configuration changes to CUB, so that the results for ICO fixed (geometry) with SOC are presented in last column.

	Cu_{13}			Ag_{13}			Au_{13}			
	2D	ICO	3D	2D	ICO	3D	2D	ICO	3D	ICO fixed
PBE	0.54	0.21	0.31	0.82	0.48	0.57	0.82	0.28	0.51	
D3	0.54	0.21	0.31	0.86	0.48	0.58	0.83	0.28	0.53	
D3BJ	0.54	0.21	0.31	0.87	0.49	0.58	0.82	0.28	0.52	
TS	0.54	0.21	0.31	0.87	0.49	0.58	0.82	0.28	0.53	
TSSCS	0.54	0.21	0.31	0.87	0.48	0.58	0.83	0.28	0.52	
MBD	0.54	0.21	0.31	0.87	0.50	0.58	0.83	0.28	0.52	
SOC	0.94	0.40	0.58	1.60	0.91	1.14	1.52	0.72	1.00	0.61
D3	0.95	0.41	0.59	1.63	0.92	1.15	1.53	0.73	1.04	0.61
D3BJ	0.95	0.41	0.59	1.65	0.94	1.15	1.53	0.72	1.00	0.61
TS	0.96	0.41	0.60	1.65	0.94	1.16	1.53	0.72	1.00	0.61
TSSCS	0.95	0.41	0.59	1.66	0.93	1.16	1.53	0.73	1.00	0.61
MBD	0.95	0.41	0.59	1.67	0.95	1.17	1.53	0.73	1.00	0.61
U_{1eV}	0.54	0.20	0.31	0.71	0.46	0.56	0.82	0.29	0.53	
D3	0.55	0.20	0.31	0.70	0.46	0.58	0.82	0.29	0.58	
D3BJ	0.55	0.20	0.31	0.71	0.46	0.57	0.82	0.29	0.53	
TS	0.55	0.21	0.31	0.72	0.46	0.57	0.81	0.29	0.56	
TSSCS	0.55	0.21	0.31	0.72	0.46	0.57	0.81	0.29	0.54	
MBD	0.55	0.21	0.31	0.72	0.47	0.57	0.82	0.29	0.53	
U_{2eV}	0.55	0.20	0.31	0.55	0.41	0.63	0.89	0.32	0.61	
D3	0.55	0.21	0.32	0.59	0.41	0.59	0.89	0.32	0.63	
D3BJ	0.55	0.21	0.31	0.55	0.42	0.64	0.90	0.32	0.61	
TS	0.54	0.21	0.31	0.56	0.42	0.62	0.90	0.32	0.62	
TSSCS	0.54	0.21	0.31	0.57	0.41	0.63	0.90	0.32	0.61	
MBD	0.55	0.21	0.31	0.58	0.43	0.65	0.89	0.32	0.61	
U_{1eV} + SOC	0.94	0.40	0.59	1.28	0.86	1.16	1.57	0.73	1.02	0.62
D3	0.96	0.40	0.59	1.32	0.85	1.23	1.57	0.73	1.05	0.62
D3BJ	0.95	0.40	0.59	1.35	0.87	1.17	1.57	0.73	1.03	0.62
TS	0.96	0.41	0.59	1.34	0.87	1.18	1.57	0.74	1.03	0.62
TSSCS	0.96	0.40	0.60	1.35	0.86	1.18	1.57	0.73	1.03	0.62
MBD	0.96	0.40	0.59	1.35	0.90	1.18	1.57	0.73	1.03	0.62
U_{2eV} + SOC	0.96	0.41	0.60	1.06	0.76	1.23	3.17	1.61	2.24	1.33
D3	0.96	0.40	0.60	1.08	0.76	1.19	3.19	1.62	2.27	1.33
D3BJ	0.96	0.40	0.61	1.11	0.80	1.26	3.19	1.66	2.27	1.33
TS	0.97	0.41	0.60	1.11	0.78	1.25	3.20	1.63	2.27	1.33
TSSCS	0.96	0.41	0.60	1.11	0.76	1.24	3.20	1.61	2.27	1.33
MBD	0.97	0.41	0.60	1.12	0.83	1.28	3.19	1.63	2.25	1.33

References

(1) Kresse, G.; Hafner, J. Ab Initio Molecular Dynamics for Open-Shell Transition Metals. *Phys. Rev. B* **1993**, *48*, 13115–13126.

(2) Kresse, G.; Furthmüller, J. Efficient Iterative Schemes for Ab Initio Total-Energy Calculations Using a Plane-Wave Basis Set. *Phys. Rev. B* **1996**, *54*, 11169–11186.

(3) Hafner, J. *Ab – initio* simulations of materials using VASP: Density-functional theory and beyond. *J. Comput. Chem.* **2008**, *29*, 2044–2078.

(4) Blöchl, P. E. Projector Augmented-Wave Method. *Phys. Rev. B* **1994**, *50*, 17953–17979.

(5) Kresse, G.; Joubert, D. From Ultrasoft Pseudopotentials to the Projector Agumented-Wave Method. *Phys. Rev. B* **1999**, *59*, 1758–1775.